

Gas excitation of post-starburst galaxies at $0.6 < z < 1.3$

A. Zanella¹, S. Belli², F. M. Valentino^{3,4}, and A. Bolamperti^{5,6}

¹ Istituto Nazionale di Astrofisica (INAF), Via Gobetti 93/3, 40129 Bologna, Italy; e-mail: anita.zanella@inaf.it

² Dipartimento di Fisica e Astronomia, Università di Bologna, Bologna, Italy

³ Cosmic Dawn Center (DAWN), Denmark

⁴ DTU Space, Technical University of Denmark, Elektrovej 327, DK-2800, Kgs. Lyngby, Denmark

⁵ Max-Planck-Institut für Astrophysik, Karl-Schwarzschild-Str. 1, D-85748 Garching, Germany

⁶ INAF – IASF Milano, via A. Corti 12, I-20133 Milano, Italy

Received XXX; accepted XXX

ABSTRACT

Context. Molecular gas in galaxies traces both the fuel for star formation and the processes that can enhance or suppress it. Observing its physical state (e.g., excitation) can therefore reveal when and why galaxies stop forming stars.

Aims. In this study, we observed the CO(5-4) emission of 8 post-starburst galaxies at $z \sim 0.6$ –1.3. To our knowledge, this is the first time that high- J transitions are probed for quiescent galaxies beyond the local Universe. All of them have detections in lower- J CO transitions (either CO(2-1) or CO(3-2)) and molecular gas fractions up to $\sim 20\%$. By studying the ratio $R_{52} = L'CO(5-4)/L'CO(2-1)$, a proxy for the gas excitation, we aim to understand how quenching occurs in these galaxies.

Methods. If significant reservoirs of molecular gas (traced by low- J CO transitions) are unable to form stars in post-starburst galaxies, low R_{52} ratios are expected, indicating reduced fractions of dense and/or warm gas relative to cold and diffuse molecular gas. Conversely, R_{52} ratios typical of main-sequence or starburst galaxies would suggest that quenching is still ongoing and that efficient star formation may rapidly exhaust the remaining molecular gas.

Results. We find that our post-starbursts have on average $R_{52} = 0.31$, comparable to high-redshift main-sequence galaxies. However, when considering only the CO(5-4) non-detections, which also coincide with post-starbursts in our sample that do not show signs of interaction, we obtain $R_{52} < 0.11$, which is 2 times lower than local star-forming galaxies and more than 2.5 times lower than high-redshift sources. The average CO Spectral Line Energy Distribution (SLED) peaks at $J = 3$, similar to the Milky Way. Three galaxies show clear signs of ongoing mergers (e.g., tidal features, companions). They have $R_{52} = 0.49$ and CO SLEDs peaking at $J \gtrsim 4$ –5, similar to high-redshift main-sequence galaxies. In at least one case additional mechanisms (e.g., AGN, shocks) are needed to explain the steep rise of the SLED up to $J = 5$.

Conclusions. The CO excitation helps distinguishing among different mechanisms responsible for the low star formation efficiency (SFE) of post-starburst galaxies. In the first scenario, the low SFE is due to the high kinetic temperatures and low gas densities that would produce high gas excitation, while in the second scenario low SFE arises from low gas densities implying low gas excitation. On average, the post-starbursts in our sample show CO excitation consistent with the second scenario. This indicates that mechanisms such as gas stabilization, feedback regulation, or stripping are needed to keep galaxies quiescent, and suggests that residual star formation is insufficient to exhaust the remaining molecular gas.

Key words. Galaxies: general - Galaxies: evolution - Galaxies: ISM

1. Introduction

Despite significant observational and theoretical efforts, the physical mechanisms quenching star formation remain under active investigation and are still a central challenge in our understanding of galaxy evolution. A plethora of different mechanisms have been proposed to stop star formation by either reducing or depleting the molecular gas reservoir or rendering the gas unable to cool and form stars (Man & Belli 2018). In particular, cold gas accretion onto the galaxy dark matter halo might be prevented (Larson et al. 1980; Feldmann & Mayer 2015; Peng et al. 2015; Feldmann et al. 2017; Davé et al. 2017) or the infalling gas might be heated up because of virial shocks (Rees & Ostriker 1977; Dekel & Birnboim 2006). In both cases, additional mechanisms are needed to prevent the cold gas reservoir that is already present in the galaxy to form new stars and to keep the galaxy quiescent. Feedback-driven outflows from active galactic nuclei (AGN) might expel the gas from the galaxy (quasar-mode feedback, Di Matteo et al. 2005) while inefficient accretion onto the

supermassive black hole (radio-mode feedback) keeps the galaxy quenched by heating the gas (Bower et al. 2006; Croton et al. 2006; Hopkins et al. 2006). Other mechanisms that have been suggested are gravitational heating due to the energy released by ram-pressure stripping (Gunn & Gott 1972; Werle et al. 2022) or dynamical friction (e.g., during the infall of a satellite or clump, Khochfar & Ostriker 2008). Gas might also be consumed by starbursts possibly triggered by major mergers (Mihos & Hernquist 1996; Springel et al. 2005; Wellons et al. 2015) and disk instabilities (Zolotov et al. 2015). However, quenching might be due to a low star formation efficiency (SFE) rather than due to the lack of fuel. The cold gas disk of galaxies might be stable against collapse and fragmentation due to the presence of a bulge (Martig et al. 2009; Johansson et al. 2009) or a stellar bar (Khoperskov et al. 2018).

Understanding what mechanisms are responsible for galaxy quenching requires identifying galaxies in the immediate aftermath of their final star-forming episode and accurately characterizing their cold gas content and physical conditions. Post-

starburst (post-SB) galaxies, also referred to as "k+a" or "e+a" systems, represent a promising population for probing this transition phase. These galaxies exhibit optical spectra dominated by strong Balmer absorption lines, indicative of A-type stars formed in a recent burst of star formation, coupled with weak or absent nebular emission lines, signaling little to no ongoing star formation (Dressler & Sandage 1983; Couch & Sharples 1987). Recent observations of low- J CO transitions such as CO(2-1) and CO(3-2), classical tracers of total cold molecular gas, have revealed significant molecular gas reservoirs in post-SB galaxies up to redshifts of $z \sim 1.4$ (French et al. 2015; Rowlands et al. 2015; Suess et al. 2017; French et al. 2018; Belli et al. 2021; Bezanson et al. 2022; Zanella et al. 2023; Suess et al. 2025). These studies report a wide variety of gas fractions that can be as high as 20%, suggesting that substantial amounts of star-forming fuel can remain in galaxies after the cessation of star formation. Despite this, post-SBs appear to lie systematically below the star-forming galaxy population in the Kennicutt–Schmidt relation, implying that their low star formation rates are not due to a lack of gas, but rather to a suppression of SFE (Zanella et al. 2023). This interpretation, however, remains tentative due to two key uncertainties: the excitation correction factor required to convert CO line luminosities to total molecular gas masses, typically assumed to be 15 – 50%, based on values from star-forming galaxies; and the obscured star formation rate (SFR), which is often inferred from mid-infrared (e.g., 24 μ m) emission. The latter can be significantly contaminated by dust heating from evolved stellar populations, particularly in post-starburst systems (Leja et al. 2019; Belli et al. 2021), complicating the accurate measurement of residual star formation activity. Probing the denser and/or warmer gas through the CO(5-4) line emission is key to estimate the gas excitation factors through the R_{52} , R_{53} ratios ($L'_{\text{CO}54}/L'_{\text{CO}21}$ and $L'_{\text{CO}32}$ ratios respectively) and unveil possible residual obscured star formation that is ongoing. In particular, if significant reservoirs of molecular gas (traced by low- J CO transitions) are unable to form stars in post-SB galaxies, R_{52} , R_{53} ratios lower than those of main-sequence galaxies are expected, i.e. reduced fractions of dense and/or warm gas over cold molecular gas. Conversely, if R_{52} , R_{53} ratios typical of main-sequence or even starburst galaxies are found it would indicate that quenching is still ongoing and that efficient star formation will likely exhaust all the remaining molecular gas on short timescales. However, observations of high- J CO transitions for quenched galaxies are still missing in the literature.

This paper is organized as follows: in Section 2 we describe the sample selection and the data set; in Section 3 we discuss how we estimated the observables (CO and dust continuum flux) and derived physical properties (molecular gas mass, R_{52} , R_{53} ratios); in Section 4 we present our results also in the context of available literature; in Section 5 we discuss the possible mechanisms that keep our galaxies quiescent and the decoupling of molecular gas and dust; finally in Section 6 we conclude and summarize our findings. Throughout the paper we adopt a flat Λ CDM cosmology with $\Omega_m = 0.3$, $\Omega_\Lambda = 0.7$, and $H_0 = 70 \text{ km s}^{-1} \text{ Mpc}^{-1}$. All magnitudes are AB magnitudes (Oke 1974) and we adopt a Chabrier (2003) initial mass function, unless otherwise stated.

2. Data

In this study we focus on 8 gas-rich post-SB galaxies at $0.6 < z < 1.3$. They were all the publicly available (to our best knowledge) and observable by ALMA $z \gtrsim 0.6$ post-SB galaxies with detected low- J CO ($J = 2, 3$) emission lines at the time when the

observations were proposed (Suess et al. 2017; Bezanson et al. 2022; Zanella et al. 2023).

2.1. Sample selection and ancillary data

The sample is extracted from two surveys: SQuIGGLE (Suess et al. 2022) and the study of Zanella et al. (2023).

The SQuIGGLE sample is selected from the Sloan Digital Sky Survey DR14 spectroscopic database (Abolfathi et al. 2018) to have strong Balmer breaks, blue slopes redward of the break, and $z \sim 0.7$. For a description of the spectroscopic identification, stellar populations, and physical characterization of SQuIGGLE galaxies we refer the reader to the survey paper (Suess et al. 2022). A subset of the SQuIGGLE sample has been observed with ALMA targeting the CO(2-1) line emission (Suess et al. 2017; Bezanson et al. 2022). Of the 13 targeted galaxies, CO(2-1) emission was detected in six. These 6 galaxies are those we focus on in this study. We note that a more recent study targeted the CO(2-1) emission of 50 additional post-SBs detecting 27 of them (Setton et al. 2025). None of them have so far published data of higher- J CO transitions. However, our sample selection and observations were concluded before this study was published.

The galaxies from Zanella et al. (2023) were initially optically selected by Wild et al. (2016) applying a principal component analysis on their spectral energy distributions (SED) based on the photometry of the Ultra-Deep Survey (Lawrence et al. 2007). The post-SB nature of a subsample of 19 objects with deep absorption lines ($\text{EW}(\text{H}\delta) > 5 \text{ \AA}$) and minimal [OII]3727 emission consistent with the unobscured SFR estimated from the UV luminosity was confirmed by Maltby et al. (2016). Two $z > 1$ targets from this subsample were targeted with ALMA by Zanella et al. (2023) and the CO(3-2) emission line was detected.

In Table 1 we report the available ALMA observations for our sample galaxies.

2.2. ALMA CO(5-4) data

We carried out ALMA Band 6 (for $z < 1$ sources) or 7 (for $z > 1$ sources) observations for our sample during Cycle 11 (Program 2024.1.00061, PI: A. Zanella) with the goal of detecting the CO(5-4) emission line at rest-frame frequency $\nu_{\text{rf}} = 576.267 \text{ GHz}$ and the underlying continuum, redshifted in the frequency range $\nu_{\text{obs}} = 260 - 360 \text{ GHz}$.

Each source was observed for 8 – 110 minutes. The sensitivities achieved are reported in Table 1. The native spectral resolution of the observations is $\sim 6.5 - 13.5 \text{ km s}^{-1}$, later binned to three times lower velocity resolutions for our purposes. The angular resolution of the observations is in the range $0.5'' - 1.4''$ (Table 1).

The data were reduced with the standard ALMA pipeline, based on the CASA software (McMullin et al. 2007). The calibrated data cubes were then converted to *uvfits* format and analyzed with the software GILDAS (Guilloteau & Lucas 2000). For consistency, we also retrieved from the ALMA archive the publicly available low- J CO data and reduced them adopting the same procedure of our CO(5-4) observations.

3. Analysis

3.1. CO(5-4) emission

To produce the velocity-integrated CO(5-4) line maps for our targets, we first determined the optimal spectral range over which to

Table 1. Log of the ALMA observations used in this work.

ID	Date	t_{exp} (min)	Noise R. M. S. mJy/beam	Beam (arcsec)	Program	Band	Line
(1)	(2)	(3)	(4)	(5)	(6)	(7)	(8)
J1448	02 Nov 2024	9	0.082	1.03×0.91	2024.1.00061.S	7	CO(5-4)
	12 Mar 2018	100	0.010	1.31×0.89	2017.1.01109.S	4	CO(2-1)
	19 Mar 2019	45	0.023	1.26×1.12	2018.1.01264.S	7	CO(4-3)
	29 Mar 2019	150	0.011	2.22×2.03	2018.1.01264.S	4	CO(2-1)
J2258	06 Nov 2024	8	0.083	1.17×0.86	2024.1.00061.S	7	CO(5-4)
	01 May 2018	100	0.009	2.34×1.99	2017.1.01109.S	4	CO(2-1)
	18 May 2021	79	0.008	0.54×0.48	2019.1.00221.S	4	CO(2-1)
ID83492	29 Oct 2024	49	0.019	1.22×1.15	2024.1.00061.S	6	CO(5-4)
	09 Jan 2020	34	0.011	1.90×1.30	2019.1.00900.S	4	CO(3-2)
J1109	07 Dec 2024	16	0.061	0.91×0.80	2024.1.00061.S	7	CO(5-4)
	10 Apr 2018	99	0.012	1.85×1.57	2017.1.01109.S	4	CO(2-1)
	19 Mar 2020	49	0.010	0.96×0.70	2019.1.00221.S	4	CO(2-1)
J1302	31 Oct 2024	17	0.066	1.08×0.86	2024.1.00061.S	7	CO(5-4)
	21 Mar 2018	100	0.013	1.07×0.98	2017.1.01109.S	4	CO(2-1)
J0912	25 Oct 2024	12	0.062	1.19×0.87	2024.1.00061.S	7	CO(5-4)
	08 Jan 2017	98	0.013	2.39×1.91	2016.1.01126.S	4	CO(2-1)
	24 Dec 2018	50	0.013	0.91×0.72	2018.1.01240.S	6	CO(4-3)
	23 Mar 2021	147	0.012	0.78×0.71	2019.1.00221.S	4	CO(2-1)
J2202	21 Oct 2024	46	0.034	0.82×0.78	2024.1.00061.S	7	CO(5-4)
	07 Mar 2017	95	0.015	3.06×2.16	2016.1.01126.S	4	CO(2-1)
ID97148	19 Nov 2024	110	0.026	1.39×1.09	2024.1.00061.S	7	CO(5-4)
	09 Jan 2020	49	0.010	1.60×1.30	2019.1.00900.S	4	CO(3-2)

Columns: (1) Galaxy ID; (2) Date of observations; (3) Integration time on source; (4) Continuum noise r. m. s.; (5) FWHM of the beam; (6) Program ID; (7) ALMA band used for the observations; (8) Targeted emission line.

Table 2. Measurements for our sample galaxies.

ID	RA (deg)	DEC (deg)	z_{CO} (4)	$S\Delta v_{\text{CO}}$ (Jy km s $^{-1}$) (5)	Δv km s $^{-1}$ (6)	L'_{CO} (10^8 K km s $^{-1}$ pc 2) (7)	F_{cont} (mJy) (8)	Line (9)
(1)	(2)	(3)	(4)	(5)	(6)	(7)	(8)	(9)
J1448	222.191344	10.169614	0.6463 ± 0.0001	0.55 ± 0.08	390 ± 52	32.6 ± 4.8	< 11.9	CO(2-1)
			0.6460 ± 0.0001	1.57 ± 0.27	307 ± 46	23.0 ± 4.0	< 58.1	CO(4-3)
			0.6465 ± 0.0002	2.62 ± 0.54	591 ± 93	24.7 ± 5.1	< 257.2	CO(5-4)
J2258	344.523653	23.221175	0.7056 ± 0.0001	1.40 ± 0.18	220 ± 24	98.1 ± 1.2	12.3	CO(2-1)
			0.7043 ± 0.0005	2.38 ± 0.75	836 ± 207	26.7 ± 8.4	< 303.1	CO(5-4)
ID83492	34.546956	-5.147125	1.1394 ± 0.0005	0.23 ± 0.09	569 ± 162	18.8 ± 7.1	< 31.9	CO(3-2)
			1.1398 ± 0.0001	0.16 ± 0.05	129 ± 34	4.6 ± 1.6	< 49.7	CO(5-4)
J1109	167.384124	-0.667679	0.5937 ± 0.0001	0.64 ± 0.06	328 ± 21	31.8 ± 2.8	< 1493.8	CO(2-1)
				< 0.33	< 2.33	< 2.6	< 156.7	CO(5-4)
J1302	195.703844	10.717528	0.5922 ± 0.0002	0.53 ± 0.08	732 ± 79	26.3 ± 3.8	< 21.8	CO(2-1)
				< 0.53	< 4.2	< 4.2	< 210.0	CO(5-4)
J0912	138.178105	15.384847	0.7472 ± 0.0001	1.01 ± 0.07	367 ± 19	79.4 ± 5.5	< 257.2	CO(2-1)
			0.7474 ± 0.0001	0.53 ± 0.11	296 ± 49	10.5 ± 2.3	< 40.8	CO(4-3)
J2202	330.601428	-0.559743	0.6582 ± 0.0001	0.24 ± 0.08	181 ± 44	14.6 ± 4.7	< 38.1	CO(2-1)
				< 2.24	< 21.9	< 21.9	< 84.2	CO(5-4)
ID97148	34.333142	-5.084108	1.2727 ± 0.0002	0.09 ± 0.05	160 ± 64	9.2 ± 4.9	< 28.6	CO(3-2)
				< 0.03	< 1.0	< 1.0	< 37.1	CO(5-4)
C1-83492*	34.547551	-5.148568	1.1374 ± 0.0002	0.79 ± 0.10	590 ± 57	71.5 ± 9.1	86.8 ± 20.1	CO(3-2)
C2-83492*	34.550126	-5.149099	1.1377 ± 0.0002	0.43 ± 0.08	388 ± 57	12.4 ± 2.4	510.4 ± 23.7	CO(5-4)

Columns: (1) Galaxy ID; (2) Right ascension of the galaxy center; (3) Declination of the galaxy center; (4) Redshift estimated by fitting the emission line with a Gaussian in our 1D ALMA spectra. The uncertainty that we report is the formal error obtained from the fit; (5) CO integrated flux density. Upper limits are 3σ ; (6) Line velocity width; (7) CO brightness temperature. Upper limits are 3σ ; (8) Flux of the continuum underlying the line. Upper limits are 3σ ; (9) CO transition.

Notes: * Indicate star-forming companions of ID83492.

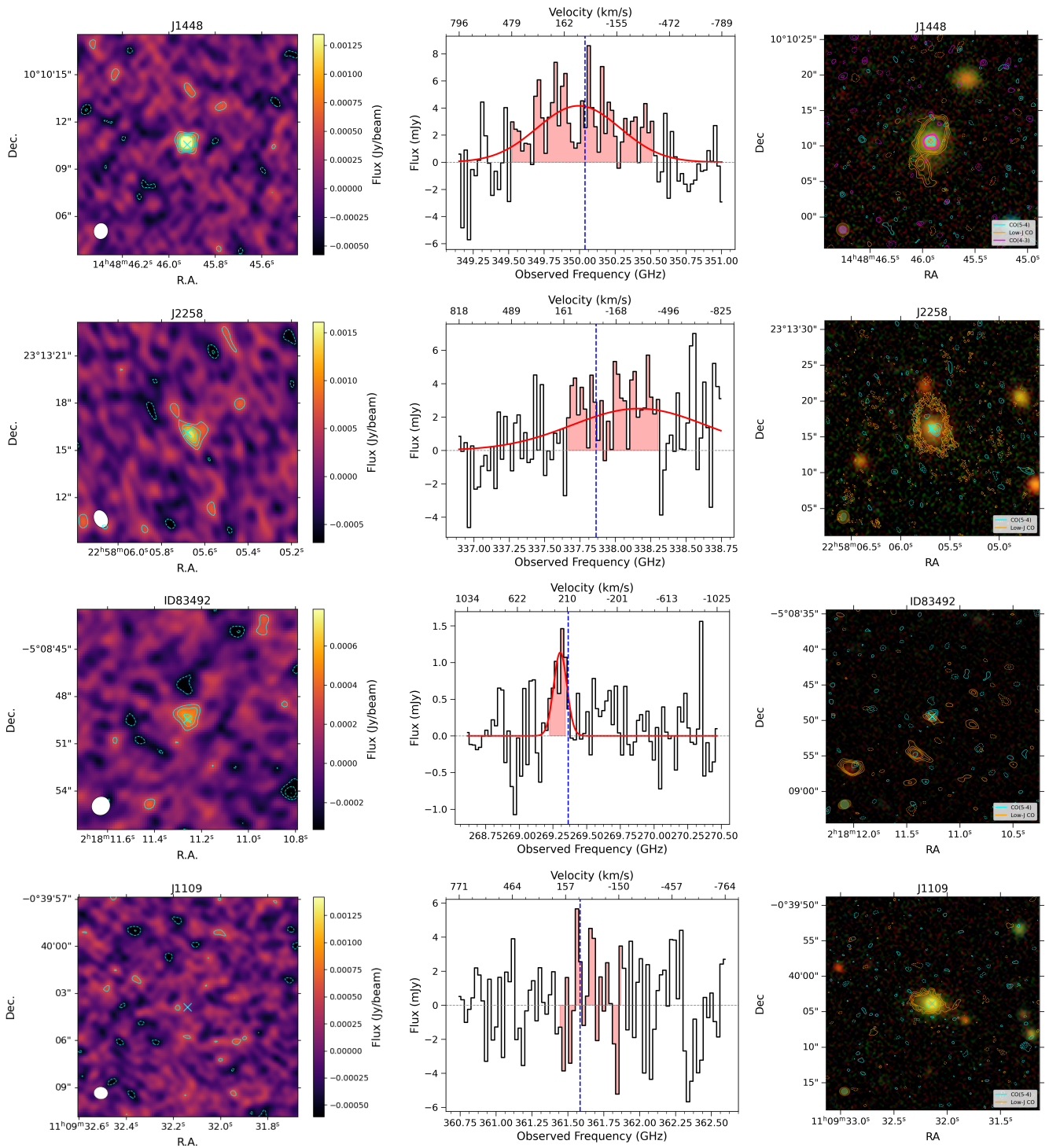


Fig. 1. ALMA data of our sample galaxies. *First column:* ALMA 2D maps of the continuum- CO(5-4) line. The cyan solid and dashed contours indicate respectively positive and negative levels of (2.5, 3.5, 4.5, 5.5) rms. The beam is reported in the bottom left corner as the white filled ellipse. Each stamp has a size of $10'' \times 10''$. The cyan cross indicates the center of our post-SB targets as estimated from the optical emission. *Second column:* 1D spectra of sources extracted using a PSF to maximize the S/N. The pink shaded areas indicate the 1σ velocity range over which we measured the CO(5-4) line flux or its upper limit. For detections we also report the Gaussian fit of the emissions (Section 3.1). The vertical dashed lines indicate the observed frequency corresponding to the redshift of the low- J CO emission. *Third column:* rest-frame optical grz images from the DESI Legacy Survey DR9 Dey et al. (2019). The cyan contours show the CO(5-4) emission, while the orange and pink indicate the low- J (CO(2-1) or CO(3-2)) or CO(4-3) emission respectively. The ellipses indicate the beam size. Each stamp has a size of $20'' \times 20''$. Contour levels are the same as in the first panels. (Continues on next page)

integrate the spectra. This was done through an iterative procedure, following an approach similar to that described in Zanella et al. (2023). We modeled the emission in the uv plane as an

elliptical Gaussian, fitting channel by channel across all four sidebands with the GILDAS task `uv_fit`. Our sources are expected to be unresolved and the size of the elliptical Gaussian

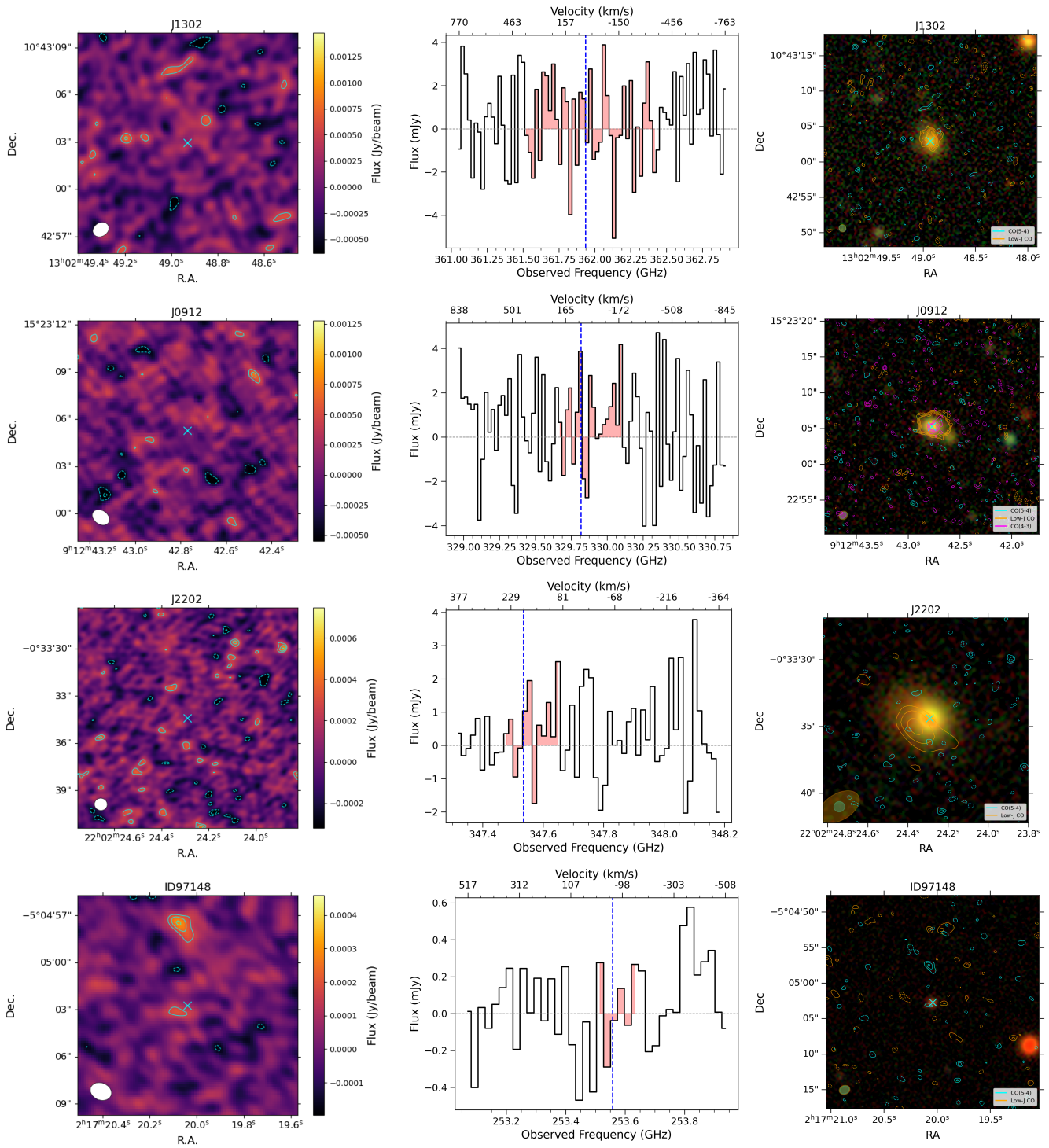


Fig. 2. ALMA data of our sample galaxies (continued). As reported in Bezanson et al. (2022), the $\sim 1''$ offset of the CO(2-1) emission of J2202 from the optical centroid is not significant given the resolution and S/N of the data. However, it is interesting to note that the optical image of this galaxy appears to be slightly asymmetric.

is indeed consistent with the beam size. Nevertheless, we chose to adopt an extended model rather than a point source, to ensure consistency with the analysis of the low- J CO emission, which in several cases is spatially resolved (Section 3.2). We verified that using a point-source model would yield CO(5-4) integrated fluxes and upper limits that are, on average, about 1.5 times fainter than those obtained with the Gaussian model. However, this difference does not affect our conclusions.

The spatial positions of the models were fixed to those derived from the CO(2-1) emission, which are consistent with the positions measured from optical imaging. Using these models, we extracted one-dimensional spectra and searched for positive line emission. When such a signal was detected, we averaged the channels that maximized the signal-to-noise ratio (S/N), and used the resulting channel-averaged two-dimensional map to fit the spatial position of the line. We considered a galaxy to be detected if its peak flux reached a significance of at least 3σ .

Table 3. Physical properties of our sample galaxies.

ID	$\log(M_\star/M_\odot)$	SFR ($M_\odot \text{ yr}^{-1}$)	$\log(M_{\text{H}_2}/M_\odot)$	sSFR (Gyr^{-1})	R_{ij}
(1)	(2)	(3)	(4)	(5)	(6)
J1448 ^a	$11.6^{+0.04}_{-0.07}$	$1.06^{+0.99}_{-0.94}$	10.3 ± 0.03	0.003	0.76 ± 0.19
J2258 ^a	$11.8^{+0.03}_{-0.05}$	$0.94^{+1.85}_{-1.71}$	10.8 ± 0.02	0.001	0.27 ± 0.09
ID83492 ^b	$10.8^{+0.20}_{-0.20}$	$0.52^{+0.79}_{-0.32}$	9.7 ± 0.10	0.008	0.24 ± 0.12^c
J1109 ^a	$11.3^{+0.09}_{-0.03}$	$2.33^{+1.12}_{-1.62}$	10.2 ± 0.03	0.012	< 0.08
J1302 ^a	$11.6^{+0.04}_{-0.06}$	$0.26^{+0.93}_{-0.26}$	10.2 ± 0.05	0.001	< 0.16
J0912 ^a	$11.2^{+0.03}_{-0.02}$	$0.81^{+1.33}_{-0.76}$	10.5 ± 0.02	0.003	< 0.05
J2202 ^a	$11.2^{+0.03}_{-0.02}$	$1.99^{+1.91}_{-1.70}$	9.8 ± 0.06	0.004	< 1.50
ID97148 ^b	$10.7^{+0.10}_{-0.10}$	< 0.72	9.6 ± 0.10	< 0.016	$< 0.11^c$
C1-83492 ^b	10.6 ± 0.1	$295.12^{+217.74}_{-225.94}$	$10.5^{+0.03}_{-0.03}$	7.9	0.19 ± 0.04^c
C2-83492 ^b	10.8 ± 0.20	$851.14^{+19.83}_{-651.61}$	$10.5^{+0.03}_{-0.03}$	13.5	0.12 ± 0.04^c

Columns: (1) ID; (2) Stellar mass from optical SED fit. We report the formal uncertainties from the SED modelling, although more realistic uncertainties accounting for systematics are ~ 0.2 dex (Pacifici et al. 2023); (3) Star formation rate from optical SED; (4) Molecular gas mass; (5) Specific star formation rate; (6) Ratio of the CO(5-4) and lower- J brightness temperature. In this table we report $R_{53} = L'_{\text{CO}(5-4)}/L'_{\text{CO}(3-2)}$ for ID83492 and ID97148, while we report $R_{52} = L'_{\text{CO}(5-4)}/L'_{\text{CO}(2-1)}$ for the rest of the sample.

Notes: ^aStellar mass, SFR, and molecular gas mass from Bezanson et al. (2022). ^bStellar mass, SFR, and molecular gas mass from Zanella et al. (2023). ^cWe report the R_{53} ratio, while in the plots we adopt a pseudo- R_{52} ratio estimated adopting $R_{32} = 0.54$ (Milky Way value, Carilli & Walter 2013).

In addition, we verified that the redshift of the detected CO line is consistent with the spectroscopic redshift from optical data and that the CO emission is spatially consistent with the optical and IR emission. We estimated the total line flux by fitting a 1D Gaussian to the extracted optimal S/N spectrum. When a line was not detected, we instead created two-dimensional maps using the channel range identified for the CO(2-1) emission and adopted a 3σ flux upper limit. We securely detected the CO(5-4) emission line for 3 galaxies, while the remaining are undetected (Figure 1).

To increase the signal-to-noise ratio for non detections we aligned the individual CO(5-4) maps to the CO(2-1) positions and stacked them (coadding visibilities). Even the stacking yielded a non detections. We estimated a CO(5-4) flux upper limit by fitting the stacked data in the uv plane with the Fourier transform of a 2D Gaussian with parameters fixed to those obtained by stacking the CO(2-1) stacking.

We estimated the redshift of the 3 detected CO(5-4) lines in two ways, both giving consistent results ($\delta z < 0.001$): by computing the signal-weighted average frequency within the line channels and by fitting the one-dimensional spectrum with a Gaussian function. We compared these redshift estimates with those obtained from CO(2-1) (Bezanson et al. 2022; Zanella et al. 2023) and found that they agree within the uncertainties. The obtained CO(5-4) total fluxes and redshifts are reported in Table 2.

3.2. Low- J CO emission

Since the main goal of this study is to compare the CO(5-4) and lower- J CO transitions, we re-analysed archival public data targeting the CO(2-1), CO(3-2), and/or CO(4-3) emission lines using the same procedure adopted for the CO(5-4) emission (Section 3.1). The fluxes we obtain are on average 20% fainter than those reported in the literature (Suess et al. 2017; Bezanson

et al. 2022; Zanella et al. 2023), due to the different models used to extract the one-dimensional spectra and measure fluxes. In particular, Suess et al. (2017) and Bezanson et al. (2022) used a circular Gaussian model with position and size allowed to vary across the line profile, whereas Zanella et al. (2023) adopted a point-source model with fixed position across the line profile. To homogenize the measurements across samples and transitions, we adopted an elliptical Gaussian model, and we report all fluxes in Table 2. A comparison of the spatial locations and morphologies of the different emission lines is shown in Figure 1.

3.3. Continuum emission

We generated averaged continuum maps by integrating over the spectral range. For the CO(5-4) detected galaxies, we excluded the channels dominated by line emission, while for the non-detections we excluded the channels where emission is expected based on the low- J CO transitions (see Section 3.2 for details). None of our main targets is detected in the $\nu_{\text{obs}} = 260\text{--}360$ GHz continuum, down to sensitivities in the range $12.6\text{--}99.3\,\mu\text{Jy}$.

We also produced continuum maps by averaging over a broader spectral range, including not only the continuum underlying the CO(5-4) line but also that associated with the lower- J transitions. This analysis likewise yielded no detections, down to sensitivities in the range $4.5\text{--}21.0\,\mu\text{Jy}$. Since no detections were found, we did not refine this analysis further, for example by assuming a continuum slope when stacking across widely different frequency ranges.

3.4. Detection of companion galaxies

Three of our sample galaxies have companions or tidal features that have been identified in low- J CO maps. We verified whether they are also detected in CO(5-4).

In particular, Zanella et al. (2023) serendipitously detected bright CO(3-2) emission lines (14.0σ and 16.5σ) and continuum (3.5σ and 4.7σ) from two galaxies in the surroundings of ID83492. Those galaxies are also detected in CO(5-4), despite having lower significance (10.6σ and 5.5σ). They both have optical counterparts in *Hubble Space Telescope* Wide Field Camera 3 (*HST*/WFC3) imaging from the 3D-HST program (Skelton et al. 2014) and their CO(5-4) redshifts are $z = 1.1377 \pm 0.0002$ and $z = 1.1380 \pm 0.0004$, consistent with the CO(2-1) redshift ($\Delta z \lesssim 0.0003$). Given their velocity offset ($v_{\text{off}} \sim 250 \text{ km s}^{-1}$ and $v_{\text{off}} \sim 195 \text{ km s}^{-1}$) and projected distance from ID83492 ($5.8'' \sim 48 \text{ kpc}$ and $13.7'' \sim 112 \text{ kpc}$), they are likely companions that might merge with our target galaxy within $< 2.5 \text{ Gyr}$, as already reported by Zanella et al. (2023). We report the properties of all companions in Table 2 and 3.

Additionally, Spilker et al. (2022) and D’Onofrio et al. (2025) have recently analyzed spatially resolved CO(2-1) maps of the J1448 and J2258 galaxies, revealing extended molecular gas tidal tails spanning up to 65 kpc, a clear indication of recent mergers. Such extended tidal features are not detected in CO(5-4) likely due to the lack of sufficient sensitivity of our data. Only a tentative ($\sim 4\sigma$) CO(5-4), spatially unresolved, emission emerges at the location of the Northern tail N3 identified by D’Onofrio et al. (2025) with CO(2-1) and $\text{H}\alpha$ emission. Its CO(5-4) redshift ($z = 0.6457 \pm 0.0003$) is consistent with that of the central body of J1448 (Table 2).

Finally, we searched for dust continuum detections nearby our targets. We report the following detections:

- four galaxies with a projected distance of $6.0'' - 15.3'' \sim 50.5 - 129.6 \text{ kpc}$ from ID83492. All of them are detected in *HST*/F160W optical imaging. The dust continuum detection of two of them, the brightest, was already reported by Zanella et al. (2023). They are also detected in CO(2-1) and CO(3-2) at a similar redshift as our main target. The remaining two do not show any emission lines in ALMA data. They have photometric redshift from 3D HST Skelton et al. (2014) $z_{\text{phot}} = 1.9808$ and $z_{\text{phot}} = 2.0229$, hence they are likely at higher redshift than our target.
- one galaxy at $9.7'' \sim 83.4 \text{ kpc}$ from ID97148 (5.4σ). This source is detected in optical VIRCAM H band data and it has several photometric redshift estimates from the literature in the range $z_{\text{phot}} = 2.0 - 2.4$ (Mehta et al. 2018; Hatfield et al. 2022), indicating that this is likely a higher redshift source than our target.
- one galaxy at $5.4'' \sim 36.8 \text{ kpc}$ from J1302 (5.4σ). The available photometric redshift estimate from the DESI survey $z_{\text{phot}} = 0.78$ (Duncan 2022) indicates that this is likely a lower redshift galaxy than J1302.

Coordinates and flux of all continuum-detected sources are reported in Table 5.

3.5. Physical properties

Stellar masses and SFR were obtained by modeling multi-wavelength photometry as described in Bezanson et al. (2022) and Zanella et al. (2023). In brief, Bezanson et al. (2022) modelled the photometry and spectra simultaneously using *Prospector* (Leja et al. 2017) with a custom set of “non parametric” star formation histories, assuming a Kriek & Conroy (2013) dust law¹. Zanella et al. (2023) modelled the photometry and the

spectra simultaneously with FAST++² (Schreiber et al. 2018) using Bruzual & Charlot (2003) models, the Chabrier (2003) IMF, delayed SFHs, the Calzetti et al. (2000) dust attenuation curve, and fixed the redshifts to the spectroscopic values. We computed the specific star formation rate as $\text{sSFR} = \text{SFR}/M_{\star}$ and report them in Table 3.

The molecular gas masses (M_{H_2}) were estimated from the CO(2-1) emission for the galaxies at $z < 1$ (Bezanson et al. 2022) and from the CO(3-2) line for the targets with $z > 1$ (Zanella et al. 2023). Both studies adopt a Milky Way-like CO-to-H₂ conversion factor (Bolatto et al. 2013). The excitation factors adopted to convert the higher J transitions to CO(1-0) are $R_{32} = 0.54$ (Carilli & Walter 2013) and $R_{21} = 1$ (Combes et al. 2007; Dannerbauer et al. 2009; Young et al. 2011). Molecular gas fractions are in the range 4% – 20%.

All our targets have available estimates of the D_n 4000 spectral index, a useful tool to constrain the mean stellar age of galaxies with younger galaxies having on average a less pronounced 4000-break (reported in Bezanson et al. 2022; Zanella et al. 2023). For the SQuIGGLE sample Bezanson et al. (2022) and Suess et al. (2021) also published an estimate of the time since quenching derived from the star formation history provided by the *Prospector* stellar population synthesis modeling.

4. Results

Observations of multiple CO transitions provide a diagnostic of the physical conditions of the molecular interstellar medium. The CO line ratios and the shape of the CO Spectral Line Energy Distribution (SLED) are sensitive to the gas volume density, kinetic temperature, and column density, thereby constraining the properties of the cold molecular gas reservoirs in galaxies (Young & Scoville 1991; Solomon & Vanden Bout 2005; Carilli & Walter 2013; Narayanan & Krumholz 2014; Bournaud et al. 2015; Popping et al. 2016; Kamenetzky et al. 2018; Combes 2018; Renaud et al. 2019b,a; Valentino et al. 2020; Liu et al. 2021).

4.1. Molecular gas excitation

By combining CO(5-4) and lower- J CO transitions, we investigated the ratios $R_{52} = L' \text{CO}(5-4)/L' \text{CO}(2-1)$ and $R_{53} = L' \text{CO}(5-4)/L' \text{CO}(3-2)$, which serve as proxies for the excitation of the molecular gas. In Figure 3, we show R_{52} as a function of sSFR for our sample of post-starbursts. For two galaxies, ID83492 and ID97148, CO(2-1) observations are not available. In these cases, we estimated $L' \text{CO}(2-1)$ from $L' \text{CO}(3-2)$ assuming the Milky Way ratio $R_{32} = 0.54$ (Weiß et al. 2005; Carilli & Walter 2013).

We also include the two star-forming companions of ID83492, as well as comparison samples of local and high-redshift main-sequence galaxies, local Ultra Luminous Infrared Galaxies (ULIRGs), and high-redshift starbursts from the literature (Liu et al. 2021). The post-SBs extend the region of parameter space sampled by star-forming galaxies toward lower sSFR. All our sample galaxies are detected in CO(2-1), while only 3 are detected in CO(5-4). Non-detections have on average a very tight upper limit $R_{52} < 0.11$ (1σ) derived by stacking (see

(2003) IMF, Bruzual & Charlot (2003) libraries, and a Calzetti et al. (2000) dust law using FAST++. The stellar masses derived from these fits are an average of 0.38 dex lower than the stellar masses derived in the default fits.

² <https://github.com/cschrreib/fastpp>

¹ They also fit the spectra and photometry with delayed exponential SFHs as described in Setton et al. (2020) assuming similar Chabrier

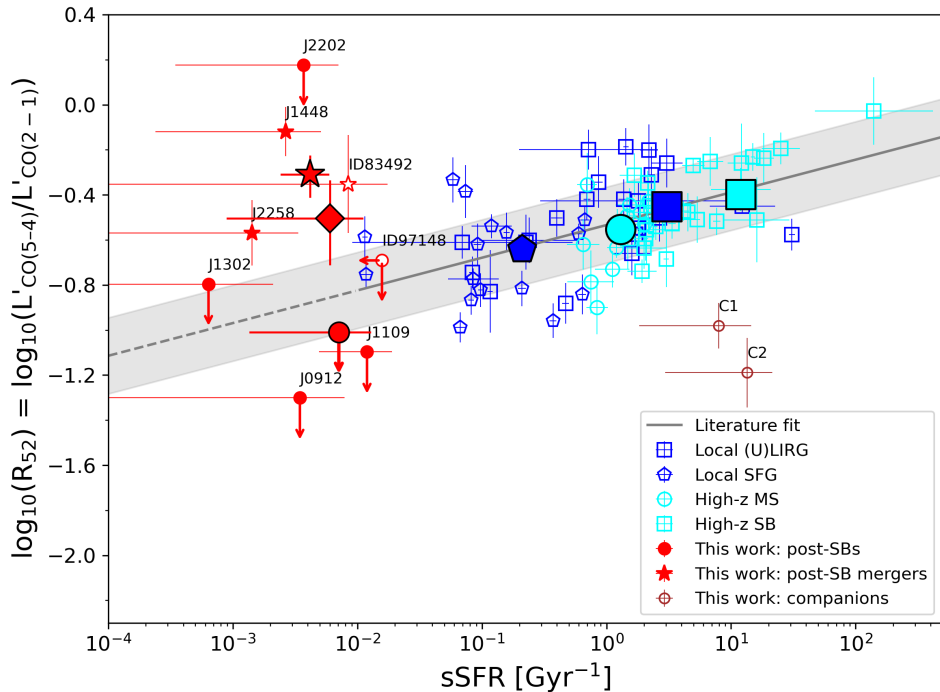


Fig. 3. Ratio of CO(5-4) to CO(2-1), a proxy for molecular gas excitation, as a function of specific star formation rate (sSFR). Our sample is shown with red circles (non mergers) and red stars (mergers) and is compared to literature samples of local star-forming galaxies (blue pentagons), local (U)LIRGs (blue squares), high-redshift main-sequence galaxies (cyan circles), and high-redshift starbursts (cyan squares; Liu et al. 2021). The two star-forming companions of ID83492 are shown as brown circles. For post-starbursts where CO(2-1) is not observed, empty symbols indicate a pseudo CO(2-1) estimated from the CO(3-2) measurement assuming the Milky Way $R_{32} = 0.54$ ratio (Carilli & Walter 2013). Large symbols indicate the population averages. The average for post-SBs without CO(5-4) detection is estimated from stacking (large red circle). The average of the whole sample of post-SBs (large red diamond) including both mergers and non mergers is derived with the Kaplan–Meier estimator from survival analysis (see text). A fit to the literature samples (gray solid line) with its scatter (gray shaded area) from Valentino et al. (2020) is shown and extrapolated toward lower sSFR (gray dashed line).

Table 4. Mean specific star formation and R_{52} ratio for our sample.

	sSFR (Gyr $^{-1}$)	R_{52}
All post-SBs	0.006	$0.31^{+0.16}_{-0.13}$
Merging post-SBs	0.004	$0.49^{+0.12}_{-0.12}$
Non merging post-SBs	0.007	< 0.11
Companions ID83492	10.716	0.08

Notes: The R_{52} is estimated as an average in case of CO(5-4) detections, namely the merging post-SBs and the companions of ID83492. The uncertainty for the merging post-SBs is estimated through bootstrap, while we do not estimate an uncertainty for the companions as they are only two. For the CO(5-4) non detections (i.e., non merging post-SBs) R_{52} is estimated through stacking (see Section 4.1). Finally, for the entire population we estimated the mean ratio using the Kaplan–Meier estimator from survival analysis to properly account for measurements and upper limits (see Section 4.1). The associated uncertainties are estimated through bootstrap.

Section 3.1). This is 2 times smaller than the average for local star-forming galaxies, and about 2.6–3.7 times lower than the R_{52} values of (U)LIRGs and high-redshift starbursts and main-sequence galaxies. This suggests a reduced fraction of dense, warm gas relative to cold, diffuse molecular gas.

The three CO(5–4) detections in our sample instead have, on average, a higher $R_{52} = 0.49$, more comparable to that of high-redshift starbursts, than the rest of the sample. We note that only the CO(5–4) detections in our sample correspond to mergers, while galaxies without detections show no evidence of companions or merger signatures (e.g., tidal tails). Their relatively high R_{52} ratio suggests that quenching is still ongoing in these systems, with star formation likely depleting the remaining molecular gas on short timescales. Such behavior indicates that gas exhaustion and potentially gas stripping are important mechanisms to keep galaxies quiescent. Interestingly, the two star-forming companions of ID83492 have sSFRs comparable to those of starburst galaxies, but their R_{52} values are lower by about 0.5 dex and comparable to the most stringent upper limits in our sample. This suggests that the ongoing merger has affected the molecular gas properties of all the galaxies involved, either depleting the warm, dense phase in the star-forming companions and/or enhancing it in the post-starburst galaxy.

Finally, we computed the average R_{52} ratio of the entire sample by employing the Kaplan–Meier estimator from survival analysis to properly account for both detections and upper limits³. We find an average $R_{52} = 0.31$ (Table 4). To estimate the associated uncertainties we employed a bootstrap resampling approach.

We also investigated whether the $L'CO(5-4)/L'CO(2-1)$ ratio correlates with other physical properties, such as the depth of the 4000 Å break, the time since quenching, or the molecular

³ We used the python package `lifelines` and the task `KaplanMeierFitter`

gas fraction. We do not find any clear correlation with any of these parameters (Figure 6). However, a larger sample with more detections is required to confirm the absence of such correlations.

In Table 4 we report the R_{52} of our sample.

4.2. Spectral line energy distribution

The CO SLED traces how the radiated energy is distributed among the different J transitions of the CO ladder and provides a powerful diagnostic of the physical conditions of the ISM. It has been shown that the CO SLED can distinguish between galaxies with low SFRs, such as the Milky Way, whose emission peaks at intermediate $J = 3-4$ (Weiß et al. 2005; Carilli & Walter 2013), and dense, warm starbursts, whose emission peaks at higher $J = 7-8$ (Weiss et al. 2007; Vallini et al. 2019; Esposito et al. 2024). In the presence of active AGN, even higher excitation is observed due to the contribution of X-ray dominated regions (van der Werf et al. 2010). Both observational (Papadopoulos et al. 2012; Daddi et al. 2015; Valentino et al. 2020; Liu et al. 2021) and theoretical studies (Narayanan & Krumholz 2014; Bournaud et al. 2015; Vollmer et al. 2017) have shown that high-redshift star-forming galaxies have higher molecular gas fractions, denser gas, and enhanced SFRs (Daddi et al. 2010; Genzel et al. 2010; Tacconi et al. 2018), resulting in CO SLEDs that peak at higher $J = 4-5$ compared to local star-forming galaxies.

By complementing our observations with archival CO(2-1), CO(3-2), and CO(4-3) data when available, we investigated the CO SLEDs of post-starbursts and compared them with literature observational and theoretical results. In Figure 4, we show the individual SLEDs of our sample galaxies, all normalized to the CO(2-1) transition. As before, for the two galaxies lacking CO(2-1) observations, we derived a pseudo CO(2-1) using $R_{32} = 0.54$ (see Section 4.1). We find a diversity of SLED shapes among our post-starbursts, with some peaking at $J \geq 5$ (e.g., J1448, J2258) and others peaking at $J = 3$ (e.g., ID97148, J0912). The average SLED of our targets peaks at $J = 4$ and exhibits a shape comparable to the Milky Way SLED (Carilli & Walter 2013).

The emission of two of the three confirmed mergers in our sample peaks at $J \geq 5$, similar to what is observed in high-redshift main-sequence galaxies (Valentino et al. 2020). For the remaining merger, only two data points are available (CO(3-2) and CO(5-4)), so additional observations are required to fully constrain the shape of its SLED.

Finally, we compared our observations with the model proposed by Narayanan & Krumholz (2014), which links a galaxy's mean SFR surface density (Σ_{SFR}), a proxy for gas density and temperature, to the shape of its CO SLED. We show in Fig. 4 the SLED predicted for $\Sigma_{\text{SFR}} = 0.05 \text{ M}_\odot \text{ yr}^{-1} \text{ kpc}^{-2}$, consistent with the average SFR surface density of our sample galaxies computed using their optical size. This model reproduces the shape of the average SLED of our post-starbursts, peaking at $J \sim 4$ and declining at higher J .

To reproduce the SLEDs of J1448 and J2258, higher Σ_{SFR} values are required. In particular, models with $\Sigma_{\text{SFR}} \sim 300 - 500 \text{ M}_\odot \text{ yr}^{-1} \text{ kpc}^{-2}$ are needed to reproduce the rising SLED of J2258 up to $J = 5$, similar to high-redshift starbursts, although additional data points at intermediate J (e.g., CO(3-2), CO(4-3)) are needed to fully constrain its shape. Instead even models with very high SFR surface densities ($\Sigma_{\text{SFR}} > 500 \text{ M}_\odot \text{ yr}^{-1} \text{ kpc}^{-2}$) struggle to reproduce the SLED of J1448, which rises steeply toward higher J transitions. The extreme shape of this SLED could be due to the presence of an AGN and/or shocks (Narayanan & Krumholz 2014). Indeed, the optical spectrum of J1448 shows

luminous and broad [OIII] and H α emission lines, indicative of AGN activity (Greene et al. 2020; D'Onofrio et al. 2025; Zhu et al. 2025), and VLA 6 GHz observations reveal a morphology consistent with compact, young radio jets (D'Onofrio et al. 2025). Additionally, shocks from AGN outflows and/or the ongoing merger may further enhance the CO excitation.

For the other two mergers in our sample, evidence for AGN activity is less clear. In J2258, D'Onofrio et al. (2025) report only faint H α emission and compact, weak radio emission consistent with past star formation. Optical and radio data for ID83492 are not available; however, it is covered by deep *Chandra* observations⁴, which also yielded no detection (Evans et al. 2024).

4.3. Residual star formation

Some works have found that a non negligible fraction ($\sim 25\%$) of local gas-rich post-starbursts host obscured star formation at levels consistent with those observed in star-forming galaxies and starbursts, thereby questioning the truly quiescent nature of some post-starbursts (Poggianti & Wu 2000; Smercina et al. 2018; Baron et al. 2022, 2023). We investigated whether (un)obscured residual star formation is present in some of our sample galaxies. Interestingly, J1448, which exhibits a 60 kpc-long CO(2-1) tidal tail (Spilker et al. 2022) due to an ongoing merger, also shows pockets of star formation traced by H α emission in the northern tail, as revealed by *HST*/WFC3 slitless spectroscopy (D'Onofrio et al. 2025). One of these H α -emitting regions also emits CO(5-4), indicating a dense molecular gas clump actively forming stars. H α and [OIII] emission are also detected in the galaxy core; however, these are consistent with AGN activity (Zhu et al. 2025; D'Onofrio et al. 2025), suggesting that the core is transitioning toward quiescence. Faint H α emission is reported in the core of J2202 as well, though it is unclear whether it originates from residual star formation or AGN activity (D'Onofrio et al. 2025). Finally, ID83492 and ID97148 both show [OII] emission in long-slit spectroscopic data, which may arise from residual star formation (dust-corrected SFR = $0.2 \pm 0.1 \text{ M}_\odot \text{ yr}^{-1}$ for ID97148 and SFR = $0.3 \pm 0.1 \text{ M}_\odot \text{ yr}^{-1}$ for ID83492; Zanella et al. 2023) or AGN activity.

To investigate the presence of obscured star formation, we converted the CO(5-4) luminosity into total IR luminosity (L_{IR}) following the relation of Valentino et al. (2020), and then converted L_{IR} into SFR using the relation from Kennicutt & De Los Reyes (2021). While undetected galaxies have relatively low SFRs ($\text{SFR} \lesssim 20 \text{ M}_\odot \text{ yr}^{-1}$), the three sources with detected CO(5-4) emission would imply significantly higher obscured SFRs ($\text{SFR} \sim 20 - 140 \text{ M}_\odot \text{ yr}^{-1}$). We verified whether such high IR luminosities are consistent with the non-detections in the dust continuum. To this end, we used the average SED template for quiescent galaxies from Magdis et al. (2021), which is characterized by a dust temperature $T_d = 20 \text{ K}$, and we rescaled it to match the most stringent dust continuum upper limit available for each galaxy. This yielded the maximum L_{IR} allowed by the lack of continuum detection, and in turn the maximum obscured SFRs ($\text{SFR} < 18 \text{ M}_\odot \text{ yr}^{-1}$), consistent with values expected for quiescent galaxies. However, Valentino et al. (2020) calibrated the CO(5-4) - L_{IR} using templates typical of high-redshift star-forming galaxies, hence with higher dust temperatures (T_d) than assumed by Magdis et al. (2021). We thus repeated the calculation using a warmer SED template ($T_d = 30 \text{ K}$) obtained by

⁴ Among the sources in our sample, only ID83492 and ID97148 are covered by deep *Chandra* observations, which did not detect them (Evans et al. 2024).

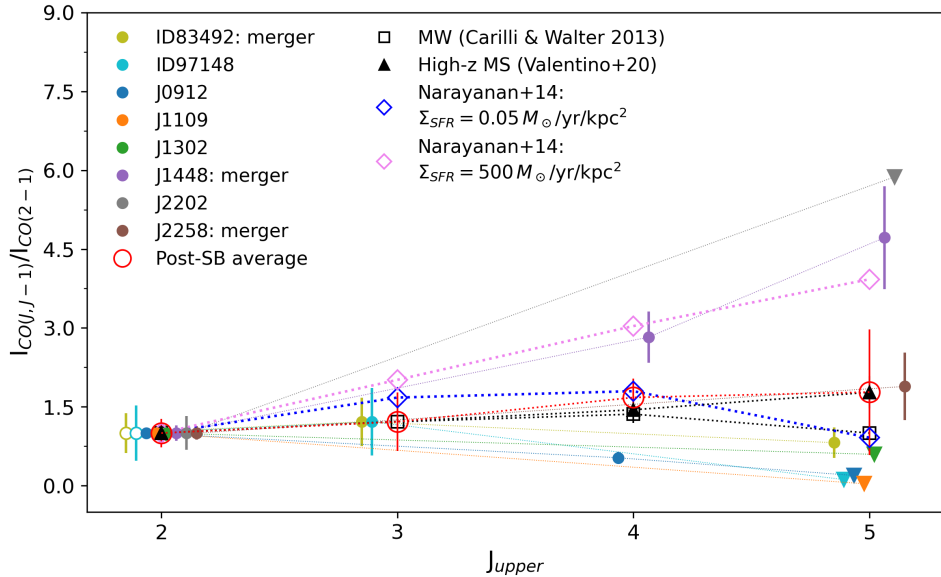


Fig. 4. CO SLED of our post-starburst galaxies. Individual galaxies are shown with small colored circles (measurements) and down-pointing triangles (3σ upper limits), while the average SLED is indicated by red empty circles. For comparison, we also show the Milky Way SLED (black squares; Carilli & Walter 2013), the average SLED of main-sequence galaxies (black triangles; Valentino et al. 2020), and the SLED predicted by the model of Narayanan & Krumholz (2014) assuming a SFR surface density of $\Sigma_{\text{SFR}} = 0.05 M_{\odot} \text{ yr}^{-1} \text{ kpc}^{-2}$ (blue diamonds) and $\Sigma_{\text{SFR}} = 500 M_{\odot} \text{ yr}^{-1} \text{ kpc}^{-2}$ (pink diamonds).

scaling the Magdis et al. (2021) SED with a modified blackbody. This yielded even lower maximum L_{IR} and even more stringent maximum obscured SFR $< 11 M_{\odot} \text{ yr}^{-1}$. In Figure 5 we compare the observed CO(5-4) luminosity for our sample galaxies with the maximum IR luminosity allowed by the dust continuum non detections, assuming the two dust temperatures described above. The measurements do not align with the CO(5-4)– L_{IR} relation that was calibrated using star-forming galaxies (Valentino et al. 2020), indicating that such a relation must be applied with caution to quiescent systems. This is also consistent with recent findings suggesting that the gas and dust in post-starburst and quiescent galaxies are decoupled, exhibiting gas-to-dust ratios that are orders of magnitude higher than in star-forming galaxies (Spilker et al. 2025). We report all the L_{IR} and SFR measurements in Table 6.

5. Discussion

The post-starburst galaxies in our sample exhibit an average $R_{52} \sim 0.31$ (from survival analysis) comparable to high-redshift star-forming galaxies. However, we find a significantly lower ratio ($R_{52} < 0.11$) when stacking only the galaxies that are not detected in CO(5-4) and that do not show signs of interaction, a value 2 times lower than local star-forming galaxies and 2.5 times lower than high-redshift main-sequence ones. This suggests a reduced fraction of dense and/or warm molecular gas relative to cold and diffuse gas in these sources, consistent with previous studies of local early-type galaxies (Crocker et al. 2012; Bayet et al. 2013) and local post-starbursts (French et al. 2023).

As highlighted by French et al. (2023), the excitation of CO-traced molecular gas can help distinguish between two potential mechanisms responsible for the low star formation efficiency observed in post-starburst galaxies. In the first scenario the low star formation efficiency is due to high kinetic temperatures combined with low gas densities, which would produce elevated gas excitation. Alternatively, high temperatures and high densities,

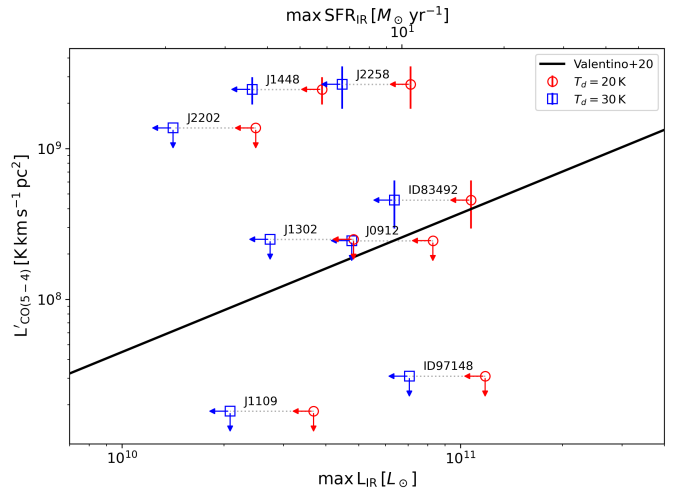


Fig. 5. CO(5-4) luminosity of our sample galaxies compared with the maximum IR luminosity allowed by the continuum non detections. We computed the maximum L_{IR} by considering the average SED template from Magdis et al. (2021) and rescaling it to match the observations. We considered both a template with dust temperature of 20 K (red circles) and 30 K (blue squares). We refer to Section 4.3 for details regarding the estimate of the IR luminosity. We overplot (black line) the CO(5-4)– L_{IR} relation estimated by Valentino et al. (2020) for star-forming galaxies that seems not to hold for our sample of post-starbursts. The top axis indicates the SFR estimated from the maximum L_{IR} with the Kennicutt & De Los Reyes (2021) conversion.

as seen in starburst galaxies, could also produce high excitation. However, in that case we would expect correspondingly high star formation rates. In the second scenario, low star formation efficiency arises from low gas densities, which would naturally lead to low gas excitation, similar to what is observed in early-type galaxies. On average, the post-starbursts in our sample exhibit CO

excitation consistent with this second scenario, indicating low gas densities and low temperatures. This result is also consistent with the local post-starburst sample analyzed by French et al. (2023), who constructed CO SLEDs up to the CO(3-2) transition.

For the three post-starbursts in our sample currently undergoing a merger, however, the situation may be different, potentially favoring the first scenario: low densities but elevated temperatures, possibly driven by shocks associated with the merging process.

The low fraction of dense molecular gas observed in most post-starburst galaxies in our sample suggests that “gas stabilization” processes, such as morphological quenching, feedback regulation, or strangulation, play a dominant role in keeping these systems quiescent and suppressing further star formation. We note, however, that our analysis is limited to post-starbursts with existing low- J CO detections, which may represent the gas-rich tail of the population. The processes responsible for shutting down star formation and those that subsequently maintain quiescence may therefore differ in gas-poor passive galaxies. Spatially resolved observations would provide stronger constraints by mapping the extent of both high- J and low- J CO emission and identifying potential spatial variations in excitation across the galaxies. In addition, higher signal-to-noise data would enable dynamical studies to assess whether the molecular gas is gravitationally stable and to search for evidence of outflows.

None of the galaxies in our sample are detected in the dust continuum, despite the fact that, based on their CO(5-4) detections and the CO(5-4) - L_{IR} relation from Valentino et al. (2020), we would have expected at least some detections. This result suggests that the CO(5-4) - L_{IR} relation established for star-forming galaxies may not hold for quiescent systems, and that molecular gas and dust could be decoupled in passive galaxies. This interpretation is consistent with recent studies reporting unexpectedly weak dust emission and unusually high gas-to-dust ratios ($\delta_{\text{GDR}} \sim 300 - 1200$; Spilker et al. 2025). These findings imply that dust continuum emission is an unreliable tracer of molecular gas in quiescent galaxies and highlight the need for alternative cold-gas diagnostics (e.g., CO). Future mid-infrared observations of post-starburst and quiescent systems will provide further insight into their spectral energy distributions, constrain their dust properties, and potentially reveal residual obscured star formation or AGN activity.

6. Summary and conclusions

We investigated the molecular gas excitation of eight post-starburst galaxies at $z \sim 0.6 - 1.3$ by comparing CO(5-4) emission with archival CO(2-1), CO(3-2), and CO(4-3) data. To our knowledge, this is the first time that high- J CO transitions are probed for quiescent galaxies at these redshifts. All galaxies in our sample are detected in low- J CO transitions and have molecular gas fractions up to $\sim 20\%$ (Bezanson et al. 2022; Zanella et al. 2023). Our main findings are as follows:

- Three out of the eight galaxies are detected in CO(5-4). All three show signs of ongoing mergers or interactions, either in the form of tidal tails (J1448 and J2258; Spilker et al. 2022; D’Onofrio et al. 2025) or via two nearby star-forming companion galaxies (ID83492; Zanella et al. 2023).
- We used the $R_{52} = L'_{\text{CO}}(5 - 4)/L'_{\text{CO}}(2 - 1)$ ratio as a proxy for molecular gas excitation. On average, our post-starburst galaxies have $R_{52} = 0.31$ (from survival analysis), comparable to high-redshift main-sequence galaxies. However, when considering only the non detections (coinciding

also with sources that do not show signs of interaction), we estimate a significantly lower $R_{52} < 0.11$ (from stacking), 2 times lower than local star-forming galaxies and > 2.5 times lower than high-redshift main-sequence and starburst galaxies. In contrast, the three merging post-starbursts exhibit higher $R_{52} \sim 0.49$, more similar to high-redshift starbursts. Interestingly, the two star-forming companions of ID83492, which have sSFRs comparable to starburst galaxies, show R_{52} values ~ 0.5 dex lower than typical main-sequence sources.

- The CO SLEDs of our post-starbursts are diverse, with an average peak at $J = 3$, similar to the Milky Way. The merging galaxies, however, have SLEDs peaking at higher J , more akin to high-redshift main-sequence galaxies, with J1448 being the most extreme case, likely requiring additional mechanisms (e.g., shocks or AGN activity) to explain its elevated excitation.
- Residual obscured star formation cannot fully account for the CO(5-4) emission in the detected galaxies, because assuming the CO(5-4) - L_{IR} relation for star-forming galaxies (Valentino et al. 2020) and the typical SED of quiescent galaxies (Magdis et al. 2021), they would have been detected in the dust continuum. Additionally, the fact that our post-starbursts do not agree with the CO(5-4) - L_{IR} relation and that none of them is detected in dust continuum indicates that molecular gas and dust in quiescent galaxies might be decoupled, as recently suggested by Spilker et al. (2025).
- Our results suggest that low gas density and temperature, leading to low CO excitation (French et al. 2023), are likely responsible for maintaining the star formation suppressed in these post-starbursts, pointing toward quenching mechanisms such as gas stabilization, stripping, or feedback regulation.

Larger samples of high-redshift post-starbursts with multi-transition CO observations will be essential to confirm and expand upon these results. Recently, Setton et al. (2025) published a sample of 50 post-SB galaxies with CO(2-1) data that could in principle be followed-up with observations of higher J CO transitions. In particular, homogeneously observing multiple CO transitions across large samples will allow statistical constraints on the SLED shapes and help determine whether elevated excitation is common in merging post-starbursts. In addition, further investigating the CO SLED of passive galaxies might shed light on the α_{CO} factor that needs to be used to convert low- J CO luminosities into molecular gas masses. Current works (e.g., French et al. 2015; French 2021; Suess et al. 2017; Bezanson et al. 2022; Zanella et al. 2023; Setton et al. 2025) typically adopt the Milky-Way conversion factor. However, α_{CO} might depend on the CO SLED of the galaxy population and could therefore be different in quiescent galaxies. Higher-resolution observations will further enable measurements of the CO-emitting region’s size, morphology, and dynamics, and help deblend close galaxy pairs, clarifying whether mergers are ubiquitous in the post-starburst population and their role in suppressing star formation at cosmic noon. Finally, assessing the presence of AGN and potential molecular outflows will be critical to understanding the contribution of AGN feedback and shocks to quenching in these galaxies.

Acknowledgements

AZ thanks F. Vito for useful discussions about the X-ray detection and possible AGN activity of our sample galaxies. SB is supported by ERC grant 101076080. FV acknowledges support from the Independent Research Fund Denmark (DFF) under grant 3120-00043B and the Danish National Research

Foundation under grant DNRF140. This paper makes use of the following ALMA data: 2016.1.01126.S; 2017.1.01109.S; 2018.1.01264.S; 2018.1.01240.S; 2019.1.00221.S; 2019.1.00900.S; 2024.1.00061.S. ALMA is a partnership of ESO (representing its member states), NSF (USA), and NINS (Japan), together with NRC (Canada), MOST and ASIAA (Taiwan), and KASI (Republic of Korea), in cooperation with the Republic of Chile. The Joint ALMA Observatory is operated by ESO, AUI/NRAO and NAOJ.

Data Availability

The data used in this study are publicly available from telescope archives. Software and derived data generated for this research can be made available upon reasonable request made to the corresponding author.

References

Abolfathi, B., Aguado, D. S., Aguilar, G., et al. 2018, *ApJS*, 235, 42
 Baron, D., Netzer, H., French, K. D., et al. 2023, *MNRAS*, 524, 2741
 Baron, D., Netzer, H., Lutz, D., Prochaska, J. X., & Davies, R. I. 2022, *MNRAS*, 509, 4457
 Bayet, E., Bureau, M., Davis, T. A., et al. 2013, *MNRAS*, 432, 1742
 Belli, S., Contursi, A., Genzel, R., et al. 2021, *ApJ*, 909, L11
 Bezanson, R., Spilker, J. S., Suess, K. A., et al. 2022, *ApJ*, 925, 153
 Bolatto, A. D., Wolfire, M., & Leroy, A. K. 2013, *ARA&A*, 51, 207
 Bournaud, F., Daddi, E., Weiß, A., et al. 2015, *A&A*, 575, A56
 Bower, R. G., Benson, A. J., Malbon, R., et al. 2006, *MNRAS*, 370, 645
 Bruzual, G. & Charlot, S. 2003, *MNRAS*, 344, 1000
 Calzetti, D., Armus, L., Bohlin, R. C., et al. 2000, *ApJ*, 533, 682
 Carilli, C. L. & Walter, F. 2013, *ARA&A*, 51, 105
 Chabrier, G. 2003, *PASP*, 115, 763
 Combes, F. 2018, *A&A Rev.*, 26, 5
 Combes, F., Young, L. M., & Bureau, M. 2007, *MNRAS*, 377, 1795
 Couch, W. J. & Sharples, R. M. 1987, *MNRAS*, 229, 423
 Crocker, A., Krips, M., Bureau, M., et al. 2012, *MNRAS*, 421, 1298
 Croton, D. J., Springel, V., White, S. D. M., et al. 2006, *MNRAS*, 365, 11
 Daddi, E., Bournaud, F., Walter, F., et al. 2010, *ApJ*, 713, 686
 Daddi, E., Dannerbauer, H., Liu, D., et al. 2015, *A&A*, 577, A46
 Dannerbauer, H., Daddi, E., Riechers, D. A., et al. 2009, *ApJ*, 698, L178
 Davé, R., Rafieferantsoa, M. H., Thompson, R. J., & Hopkins, P. F. 2017, *MNRAS*, 467, 115
 Dekel, A. & Birnboim, Y. 2006, *MNRAS*, 368, 2
 Dey, A., Schlegel, D. J., Lang, D., et al. 2019, *AJ*, 157, 168
 Di Matteo, T., Springel, V., & Hernquist, L. 2005, *Nature*, 433, 604
 D’Onofrio, V. R., Spilker, J. S., Bezanson, R., et al. 2025, arXiv e-prints, arXiv:2507.21249
 Dressler, A. & Sandage, A. 1983, *ApJ*, 265, 664
 Duncan, K. J. 2022, *MNRAS*, 512, 3662
 Esposito, F., Vallini, L., Pozzi, F., et al. 2024, *MNRAS*, 527, 8727
 Evans, I. N., Evans, J. D., Martínez-Galarza, J. R., et al. 2024, *ApJS*, 274, 22
 Feldmann, R. & Mayer, L. 2015, *MNRAS*, 446, 1939
 Feldmann, R., Quataert, E., Hopkins, P. F., Faucher-Giguère, C.-A., & Kereš, D. 2017, *MNRAS*, 470, 1050
 French, K. D. 2021, *PASP*, 133, 072001
 French, K. D., Smercina, A., Rowlands, K., et al. 2023, *ApJ*, 942, 25
 French, K. D., Yang, Y., Zabludoff, A., et al. 2015, *ApJ*, 801, 1
 French, K. D., Yang, Y., Zabludoff, A. I., & Tremonti, C. A. 2018, *ApJ*, 862, 2
 Genzel, R., Tacconi, L. J., Gracia-Carpio, J., et al. 2010, *MNRAS*, 407, 2091
 Greene, J. E., Setton, D., Bezanson, R., et al. 2020, *ApJ*, 899, L9
 Guilloteau, S. & Lucas, R. 2000, in *Astronomical Society of the Pacific Conference Series*, Vol. 217, *Imaging at Radio through Submillimeter Wavelengths*, ed. J. G. Mangum & S. J. E. Radford, 299
 Gunn, J. E. & Gott, J. Richard, I. 1972, *ApJ*, 176, 1
 Hatfield, P. W., Jarvis, M. J., Adams, N., et al. 2022, *MNRAS*, 513, 3719
 Hopkins, P. F., Somerville, R. S., Hernquist, L., et al. 2006, *ApJ*, 652, 864
 Johansson, P. H., Naab, T., & Ostriker, J. P. 2009, *ApJ*, 697, L38
 Kamenetzky, J., Privon, G. C., & Narayanan, D. 2018, *ApJ*, 859, 9
 Kennicutt, Jr., R. C. & De Los Reyes, M. A. C. 2021, *ApJ*, 908, 61
 Khochfar, S. & Ostriker, J. P. 2008, *ApJ*, 680, 54
 Khoperskov, S., Haywood, M., Di Matteo, P., Lehnert, M. D., & Combes, F. 2018, *A&A*, 609, A60
 Kriek, M. & Conroy, C. 2013, *ApJ*, 775, L16
 Larson, R. B., Tinsley, B. M., & Caldwell, C. N. 1980, *ApJ*, 237, 692
 Lawrence, A., Warren, S. J., Almaini, O., et al. 2007, *MNRAS*, 379, 1599
 Leja, J., Carnall, A. C., Johnson, B. D., Conroy, C., & Speagle, J. S. 2019, *ApJ*, 876, 3
 Leja, J., Johnson, B. D., Conroy, C., van Dokkum, P. G., & Byler, N. 2017, *ApJ*, 837, 170
 Liu, D., Daddi, E., Schinnerer, E., et al. 2021, *ApJ*, 909, 56
 Magdis, G. E., Gobat, R., Valentino, F., et al. 2021, *A&A*, 647, A33
 Malby, D. T., Almaini, O., Wild, V., et al. 2016, *MNRAS*, 459, L114
 Man, A. & Belli, S. 2018, *Nature Astronomy*, 2, 695
 Martig, M., Bournaud, F., Teyssier, R., & Dekel, A. 2009, *ApJ*, 707, 250
 McMullin, J. P., Waters, B., Schiebel, D., Young, W., & Golap, K. 2007, in *Astronomical Society of the Pacific Conference Series*, Vol. 376, *Astronomical Data Analysis Software and Systems XVI*, ed. R. A. Shaw, F. Hill, & D. J. Bell, 127
 Mehta, V., Scarlata, C., Capak, P., et al. 2018, *ApJS*, 235, 36
 Mihos, J. C. & Hernquist, L. 1996, *ApJ*, 464, 641
 Narayanan, D. & Krumholz, M. R. 2014, *MNRAS*, 442, 1411
 Oke, J. B. 1974, *ApJ*, 189, L47
 Pacifici, C., Iyer, K. G., Mobasher, B., et al. 2023, *ApJ*, 944, 141
 Papadopoulos, P. P., van der Werf, P. P., Xilouris, E. M., et al. 2012, *MNRAS*, 426, 2601
 Peng, Y., Maiolino, R., & Cochrane, R. 2015, *Nature*, 521, 192
 Poggianti, B. M. & Wu, H. 2000, *ApJ*, 529, 157
 Popping, G., van Kampen, E., Decarli, R., et al. 2016, *MNRAS*, 461, 93
 Rees, M. J. & Ostriker, J. P. 1977, *MNRAS*, 179, 541
 Renaud, F., Bournaud, F., Agertz, O., et al. 2019a, *A&A*, 625, A65
 Renaud, F., Bournaud, F., Daddi, E., & Weiß, A. 2019b, *A&A*, 621, A104
 Rowlands, K., Wild, V., Nesvadba, N., et al. 2015, *MNRAS*, 448, 258
 Schreiber, C., Glazebrook, K., Nanayakkara, T., et al. 2018, *A&A*, 618, A85
 Setton, D. J., Bezanson, R., Suess, K. A., et al. 2020, *ApJ*, 905, 79
 Setton, D. J., Spilker, J. S., Bezanson, R., et al. 2025, arXiv e-prints, arXiv:2509.00148
 Skelton, R. E., Whitaker, K. E., Momcheva, I. G., et al. 2014, *ApJS*, 214, 24
 Smercina, A., Smith, J. D. T., Dale, D. A., et al. 2018, *ApJ*, 855, 51
 Solomon, P. M. & Vanden Bout, P. A. 2005, *ARA&A*, 43, 677
 Spilker, J. S., Suess, K. A., Setton, D. J., et al. 2022, *ApJ*, 936, L11
 Spilker, J. S., Whitaker, K. E., Narayanan, D., et al. 2025, arXiv e-prints, arXiv:2507.16914
 Springel, V., Di Matteo, T., & Hernquist, L. 2005, *ApJ*, 620, L79
 Suess, K. A., Beverage, A. G., Kriek, M., et al. 2025, arXiv e-prints, arXiv:2506.14361
 Suess, K. A., Bezanson, R., Spilker, J. S., et al. 2017, *ApJ*, 846, L14
 Suess, K. A., Kriek, M., Bezanson, R., et al. 2022, *ApJ*, 926, 89
 Suess, K. A., Kriek, M., Price, S. H., & Barro, G. 2021, *ApJ*, 915, 87
 Tacconi, L. J., Genzel, R., Saintonge, A., et al. 2018, *ApJ*, 853, 179
 Valentino, F., Daddi, E., Puglisi, A., et al. 2020, *A&A*, 641, A155
 Vallini, L., Tielens, A. G. G. M., Pallottini, A., et al. 2019, *MNRAS*, 490, 4502
 van der Werf, P. P., Isaak, K. G., Meijerink, R., et al. 2010, *A&A*, 518, L42
 Vollmer, B., Gratier, P., Braine, J., & Bot, C. 2017, *A&A*, 602, A51
 Weiss, A., Downes, D., Walter, F., & Henkel, C. 2007, in *Astronomical Society of the Pacific Conference Series*, Vol. 375, *From Z-Machines to ALMA: (Sub)Millimeter Spectroscopy of Galaxies*, ed. A. J. Baker, J. Glenn, A. I. Harris, J. G. Mangum, & M. S. Yun, 25
 Weiß, A., Walter, F., & Scoville, N. Z. 2005, *A&A*, 438, 533
 Wellons, S., Torrey, P., Ma, C.-P., et al. 2015, *MNRAS*, 449, 361
 Werle, A., Poggianti, B., Moretti, A., et al. 2022, *ApJ*, 930, 43
 Wild, V., Almaini, O., Dunlop, J., et al. 2016, *MNRAS*, 463, 832
 Young, J. S. & Scoville, N. Z. 1991, *ARA&A*, 29, 581
 Young, L. M., Bureau, M., Davis, T. A., et al. 2011, *MNRAS*, 414, 940
 Zanella, A., Valentino, F., Gallazzi, A., et al. 2023, *MNRAS*, 524, 923
 Zhu, P., Suess, K. A., Kriek, M., et al. 2025, *ApJ*, 981, 60
 Zolotov, A., Dekel, A., Mandelker, N., et al. 2015, *MNRAS*, 450, 2327

7. Appendix

Continuum detections

We searched for dust continuum detections nearby our targets and found several targets. We report in Table 5 their coordinates and fluxes.

Table 5. Coordinates and continuum flux of the sources serendipitously detected nearby our targets.

ID	RA (deg)	Dec (deg)	F_{cont} (μJy)
ID83492-cont1	34.548128	-5.151115	67.4 ± 1.0
ID83492-cont2	34.549892	-5.144405	72.0 ± 14.7
ID97148-cont1	34.332948	-5.081456	71.0 ± 13.2
J1302-cont1	195.704078	10.718890	87.7 ± 16.2

Molecular gas excitation

We investigated possible correlations between the CO(5–4)/CO(2–1) luminosity ratio and several galaxy properties, namely the 4000 Å break strength (Dn4000), the quenching timescale (t_q), and the molecular gas fraction (M_{H_2}/M_{\star}), as shown in Fig. 6. To quantify any trends, we computed both the Pearson and Spearman correlation coefficients. In all cases, we found no statistically significant correlations: for Dn4000, $r_P = 0.27$ ($p = 0.52$); for t_q , $r_P = -0.30$ ($p = 0.56$); and for M_{H_2}/M_{\star} , $r_P = -0.33$ ($p = 0.43$). The corresponding Spearman coefficients are similarly low ($|r_S| < 0.5$) with $p > 0.3$. These results indicate that, within the current uncertainties and limited sample size, there is no compelling evidence for a correlation between the CO excitation (as traced by R_{52}) and stellar population age, quenching timescale, or gas content.

Residual obscured star formation

We investigated whether our sample galaxies had residual star formation by converting the CO(5–4) luminosity into total IR luminosity following the relation of Valentino et al. (2020). We then converted the L_{IR} into SFR by using the Kennicutt & De Los Reyes (2021) relation (see Section 4.3 for details). We also computed the maximum L_{IR} consistent with the dust continuum non detection considering the average SED template for quiescent galaxies from Magdis et al. (2021) both with a dust temperature of 20 K and 30 K. In Table 6 we report the L_{IR} and SFR obtained with the different methods.

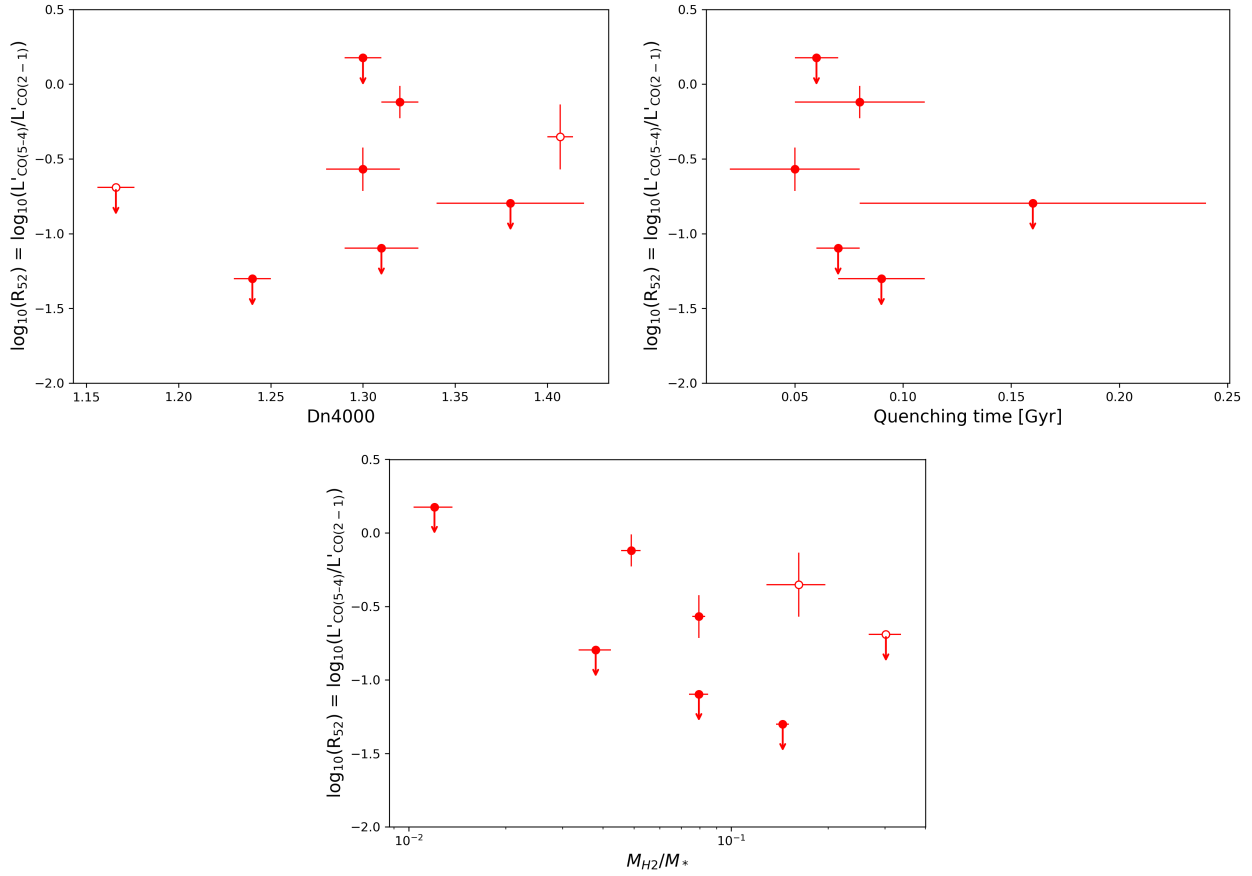


Fig. 6. Molecular gas excitation traced by the CO(5-4)/CO(2-1) brightness temperature ratio (R_{52}) as a function of galaxy properties. *Top left*: R_{52} versus the 4000Å break. *Top right*: R_{52} versus the time since quenching. *Bottom*: R_{52} versus the molecular gas fraction.

Table 6. IR luminosity and star formation rate obtained (i) converting the CO(5-4) luminosity into L_{IR} using the Valentino et al. (2020) relation ($L_{\text{IR},V20}$, SFR_{V20}); (ii) considering the observed continuum upper limits and the average SED template for quiescent galaxies from Magdis et al. (2021). We considered both a template dust temperature of 20 K ($L_{\text{IR},20\text{K}}$, $\text{SFR}_{20\text{K}}$) and 30 K ($L_{\text{IR},30\text{K}}$, $\text{SFR}_{30\text{K}}$).

ID	$L_{\text{IR},V20}$ ($10^{10} L_{\odot}$)	SFR_{V20} ($M_{\odot} \text{ yr}^{-1}$)	$L_{\text{IR},20\text{K}}$ ($10^{10} L_{\odot}$)	$\text{SFR}_{20\text{K}}$ ($M_{\odot} \text{ yr}^{-1}$)	$L_{\text{IR},30\text{K}}$ ($10^{10} L_{\odot}$)	$\text{SFR}_{30\text{K}}$ ($M_{\odot} \text{ yr}^{-1}$)
J1448	78.4 ± 17.6	116.7 ± 26.3	< 3.9	< 5.8	< 2.4	< 3.6
J2258	85.3 ± 29.1	127.1 ± 43.3	< 7.1	< 10.6	< 4.5	< 6.7
ID83492	12.5 ± 4.8	18.6 ± 7.1	< 10.8	< 16.0	< 6.4	< 9.5
J1109	< 2.0	< 2.9	< 3.7	< 5.5	< 2.1	< 3.1
J1302	< 3.9	< 5.9	< 4.8	< 7.2	< 2.7	< 4.1
J0912	< 3.7	< 5.5	< 8.3	< 12.3	< 4.8	< 7.1
J2202	< 23.9	< 25.6	< 2.5	< 3.7	< 1.4	< 2.1
ID97148	< 0.8	< 1.2	< 11.8	< 17.6	< 7.1	< 10.5